

Decameter Cropland LAI/FPAR Estimation From Sentinel-2 Imagery Using Google Earth Engine

Yuanheng Sun^{ID}, Qiming Qin, Huazhong Ren^{ID}, and Yao Zhang

Abstract—Leaf area index (LAI) and fraction of photosynthetically active radiation (FPAR) products at regional and global scales have already been extensively and routinely generated from medium-resolution sensors. However, there is a lack of high-resolution LAI/FPAR product, which is especially essential for crop growth and drought monitoring of cropland in patches. This article proposes a processing framework for the derivation of decameter cropland LAI and FPAR in the Northern China plain from Sentinel-2 surface reflectance data with a random forest (RF) algorithm by exploiting the capabilities of the Google Earth Engine (GEE) cloud platform. The training database is generated from the spatially aggregated Sentinel-2 surface reflectance and the corresponding Moderate Resolution Imaging Spectroradiometer (MODIS) LAI/FPAR product over homogeneous cropland, and the training samples are strictly filtered for the best quality. RF is then trained over the processed Sentinel-2 surface reflectance and the filtered MODIS LAI/FPAR under two input groups—one group is for Sentinel-2 spectral bands of 10-m resolution only, and the other group supplements the Sentinel-2 red-edge (RE) and shortwave infrared (SWIR) bands of 20-m resolution. Extensive comparisons and validation are carried out, and they demonstrate that the new method can generate spatial and temporal consistent LAI/FPAR with MODIS at high spatial resolution. The retrieval accuracy is slightly better for 20-m input groups than that for 10-m input groups, confirming the value of RE and/or SWIR in cropland LAI/FPAR estimate. This article also demonstrates that GEE is a suitable high-performance processing tool for high-resolution biophysical variables estimation.

Index Terms—Cropland, fraction of photosynthetically active radiation (FPAR), Google Earth Engine (GEE), leaf area index (LAI), Moderate Resolution Imaging Spectroradiometer (MODIS), Sentinel-2.

I. INTRODUCTION

THE world's population is projected to be 10 billion by the year 2050, which was estimated by Food and Agriculture

Manuscript received August 17, 2020; revised December 14, 2020; accepted January 13, 2021. This work was supported in part by the National Natural Science Foundation of China under Grant 41771371, Grant 41701434, and Grant 41801245, in part by China High-Resolution Earth Observation System (CHEOS) under Grant 11-Y20A16-9001-17/18, and in part by China Scholarship Council under Grant 201906010045. (*Corresponding authors:* Qiming Qin; Huazhong Ren.)

Yuanheng Sun and Huazhong Ren are with the Institute of Remote Sensing and Geographic Information System, Peking University, Beijing 100871, China (e-mail: yhsun@pku.edu.cn; renhuazhong@pku.edu.cn).

Qiming Qin is with the Institute of Remote Sensing and Geographic Information System, Peking University, Beijing 100871, China, and also with the Beijing Key Laboratory of Spatial Information Integration and 3S Application, Peking University, Beijing 100871, China (e-mail: qmqin@pku.edu.cn).

Yao Zhang is with the Key Laboratory of Modern Precision Agriculture System Integration Research, Ministry of Education, China Agricultural University, Beijing 100083, China (e-mail: zhangyao@cau.edu.cn).

Color versions of one or more figures in this article are available at <https://doi.org/10.1109/TGRS.2021.3052254>.

Digital Object Identifier 10.1109/TGRS.2021.3052254

Organization (FAO) of the United Nation (UN) [1], and it boosts great agricultural demand for food security. The increase in food production must be accompanied by a sustainable management of agricultural lands, which requires the dynamic and massive monitoring and forecasting of crop growing status and yields [2]. Remote sensing appears as an essential tool to respond to the abovementioned requirements since it offers a nondestructive mean of providing recurrent information from the local to the global scale in a systematic way, thereby enabling the characterization of the spatial and temporal variability within a given region.

Leaf area index (LAI) and fraction of photosynthetically active radiation (FPAR) are of the greatest importance among those parameters, which are related to crop-growing status and yields. LAI is a canopy structure parameter and is defined as the total one-sided area of photosynthetic tissue per unit ground area [3]. FPAR quantifies the fraction of the solar radiation absorbed by live leaves in the spectral range of 400–700 nm for the photosynthesis activities [4], [5].

Optical remote sensing data is widely used for LAI and FPAR estimation; it can be categorized into empirical and physical ones by the major methods. Empirical methods establish the relationship between satellite-derived reflectance or vegetation indices and LAI/FPAR using statistical regression or advanced nonparametric models [6]–[8]. It is easy to implement but requires calibrations for different vegetation types with huge field observations, thus is mostly applied in local applications [9]. The radiative transfer (RT) equation naturally links the radiation intensity measured by satellite-borne sensors and the land surface vegetation parameters by describing the motion of photons within the canopies, and that is why it is named as physical [5], [10]. Vegetation variables are retrieved with RT model inversion by taking sensor-measured intensity or reflectance and other auxiliary information as inputs. Such an inversion process is quite computational demanding, thus many retrieval techniques, such as lookup table (LUT) [11], [12] and machine learning algorithms [13]–[15], are implemented to speed up this process.

A variety of global LAI/FPAR products are derived from various satellite data using the abovementioned methods. The majority of those LAI/FPAR products, represented by Moderate Resolution Imaging Spectroradiometer (MODIS) [11], Carbon CYCLE and Change in Land Observational Products from an Ensemble of Satellites (CYCLOPS) [15], and Geoland2/BioPar version (GEOV) [13], are mainly in coarse spatial resolution of 300 m–8 km and the temporal interval

of 4–16 days, which are suitable for large-scale long-term monitoring of natural vegetation; however, they are not adequate for cropland monitoring especially when the cropland is in patches or fast-growing stages. High-resolution satellite data, such as Landsat TM/ETM+/OLI, which is suitable for local to regional cropland monitoring, does not have sustained and consistent LAI/FPAR product for ready-to-use directly. Besides, a single Landsat satellite has a quite long revisit period, that is, 16 days, under the cloudless circumstance, results in the missing of extensive crop information during fast-growing stages.

The emergence of Sentinel-2 effectively meets the demands of spatial and temporal resolution in the process of cropland monitoring. Sentinel-2 is a wide-swath, high-resolution, and multispectral imaging mission supporting the European Space Agency (ESA) Copernicus Land Monitoring studies, which was launched in 2015 (Sentinel-2A) and 2017 (Sentinel-2B) [16]. It provides up to 10-m resolution visible to shortwave infrared (SWIR) spectral bands in a five-day revisit period, thus is of great benefit to crop LAI/FPAR retrieval and growth monitoring [17]. On the other hand, high spatial and temporal resolution brings in high computational demand, and local personal computers and small servers cannot undertake the operational regional and global data computation timely. Google Earth Engine (GEE) offers us a free and convenient cloud-computing platform for geospatial analysis at the petabyte scale [18], which dramatically speeds up the data processing efficiency. Numerous regional and global remote sensing applications have been conducted on GEE, which includes land cover mapping [19], [20], vegetation monitoring [21], [22], land surface temperature estimation [23], and hydrological process [24], [25].

A high-resolution cropland LAI/FPAR map, which is spatially and temporally consistent with those medium-resolution LAI/FPAR products, is of great benefit and urgent demand for agricultural applications. As such, the goal of this work is to establish a retrieval chain for decameter LAI/FPAR in Northern China plain cropland from Sentinel-2 surface reflectance data on the GEE platform. The retrieval algorithm is a random forest (RF) regression and is trained with spatial and temporal representative best-quality MODIS LAI/FPAR values in homogeneous cropland. The retrieved LAI/FPAR values are compared to the original MODIS products, and the LAI is also validated by the ground measurements.

The organization of this article is as follows. Section II describes the study area and data sets, which include Sentinel-2, FROM-GLC, and MODIS LAI/FPAR products. Detailed descriptions regarding the implementation of the retrieval algorithm, including the selection of the best-quality training samples, are described in Section III. Validation and comparisons of the LAI/FPAR retrieved from Sentinel-2 surface data by the proposed method with the original MODIS LAI/FPAR products and ground measurements are presented in Section IV. Section V discusses the method applicability, causes of uncertainty, and remaining issues to be improved. This article concludes in Section VI with a summary of the results.

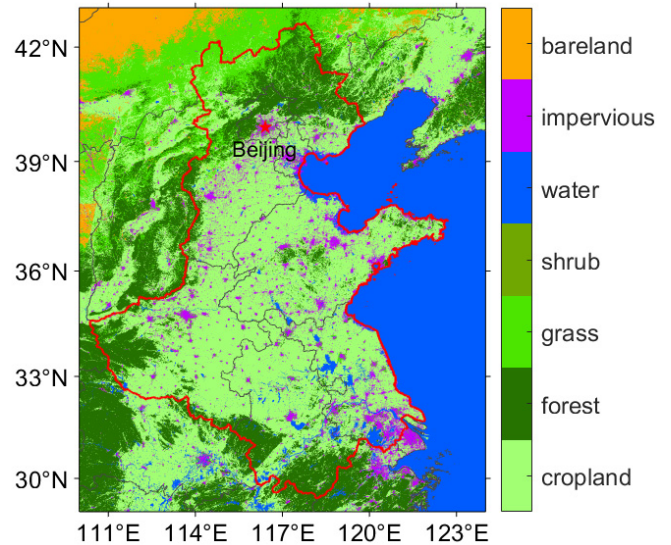


Fig. 1. Location of the study area, including Hebei, Henan, Shandong, Jiangsu, Anhui, Beijing, and Tianjin outlined with red boundary. The background image is from FROM-GLC10 land cover data set.

II. STUDY AREA AND DATA SET

A. Study Area

Our study area contains five provinces and two municipalities, including Hebei, Henan, Shandong, Jiangsu, Anhui, Beijing, and Tianjin, of China across the Northern China plain. The spatial extent of the study area is 29° N–43° N and 110° E–123° E, which is illustrated in Fig. 1. We focus on the cropland on the plain over the study area only, and it is extracted based on the FROM-GLC10 land cover data set (detail description of data set in Section II-B) with an overall area over 300 000 km². The region has a temperate and warm temperate monsoon (wet summer and dry winter) climate with an average annual temperature of 11 °C–15 °C and an average annual precipitation of 500–900 mm. Winter wheat (*Triticum aestivum L.*) and maize (*Zea mays L.*) are the main crops in this region, which are under rotation irrigated management practices. Wheat is sowed in October and harvested in May of next year, while maize is cultivated from June to September on average [9], [26].

B. Data Set

1) *Sentinel-2*: The Multispectral Instrument (MSI) boarded on Sentinel-2 satellite acquires data in 13 spectral bands including visible, near-infrared, and SWIR ranges with a spatial resolution of 10–60 m and a five-day revisit period when Sentinel-2A and Sentinel-2B are combined under cloudless circumstances [16]. The detailed information of the Sentinel-2 band setting is listed in Table I. Level-2A surface reflectance data set of Sentinel-2 is used in this study as the inputs of LAI/FPAR retrieval chain.

2) *FROM-GLC*: Finer Resolution Observation and Monitoring of Global Land Cover (FROM-GLC) product in 10-m resolution for the year of 2017 was used to delineate cropland in this article over our study area. FROM-GLC10 is an updated version of FROM-GLC30 (30-m resolution) with a stable classification accuracy, achieved by transferring a 30-m resolution

TABLE I
BAND INFORMATION OF SENTINEL-2A/MSI

Band	Central wavelength (nm)	Band width (nm)	Spatial resolution (m)
B1-Coastal	443	20	60
B2-Blue	490	65	10
B3-Green	560	35	10
B4-Red	665	30	10
B5-Red edge 1	705	15	20
B6-Red edge 2	740	15	20
B7-Red edge 3	783	20	20
B8-NIR	842	115	10
B8A-NIR	865	20	20
B9-Water vapor	945	20	60
B10-Cirrus	1375	30	60

sample set and adding Sentinel-2 data set by using an RF classifier in the GEE platform [27]. FROM-GLC10 shows more spatial detail than any other courser resolution land cover product, and it is the latest land cover map that matches the 10-m spatial resolution of Sentinel-2 over our study area. In addition, 64.39% of the study area is covered by cropland, and the percentages of forest, grass or shrub, imperious, and water are 18.31%, 5.37%, 8.28%, and 3.65%, respectively.

3) MODIS LAI/FPAR Product: The latest Collection 6 (C6) Terra and Aqua MODIS LAI/FPAR products (MCD15A3H) are used in this study for LAI/FPAR training data set generation. MCD15A3H provides four-day composite 500-m resolution LAI/FPAR product in Sinusoidal projection. The main algorithm of the products is based on the 3-D RT equation, which links the surface spectral bidirectional reflectance factors (BRFs) to structural and spectral parameters of the vegetation canopy, and the backup empirical algorithm is based on biome-specific relations between the normalized difference vegetation index (NDVI) and LAI/FPAR [5], [11], [28]. The method chooses the high-quality pixel generated with the main algorithm available from all the acquisitions of both MODIS sensors located on NASA's Terra and Aqua satellites from within the four-day period. The quality of this data set was comprehensively evaluated against ground-based measurements and through intercomparisons with other satellite LAI/FPAR products, with root-mean-square errors (RMSEs) of 0.66 and 0.15 for LAI and FPAR against ground-based measurements for all biome types, respectively [29].

III. METHODOLOGY

The retrieval method proposed in this study employs the RF machine learning algorithm embedded in GEE to retrieve Sentinel-2 LAI/FPAR from its L2A surface reflectance data set. High-quality MCD15 LAI and FPAR are used as the output variables during the model training process. The whole retrieval chain comprises four steps, which includes Sentinel-2 pixels screening, MODIS pixels screening, training samples generation, and LAI/FPAR retrieval. A schematic flowchart outlining the method is shown in Fig. 2.

A. Sentinel-2 Pixels Screening

Sentinel-2 pixels screening aims to retain the best-quality homogeneous cropland pixels and filter out noncropland and

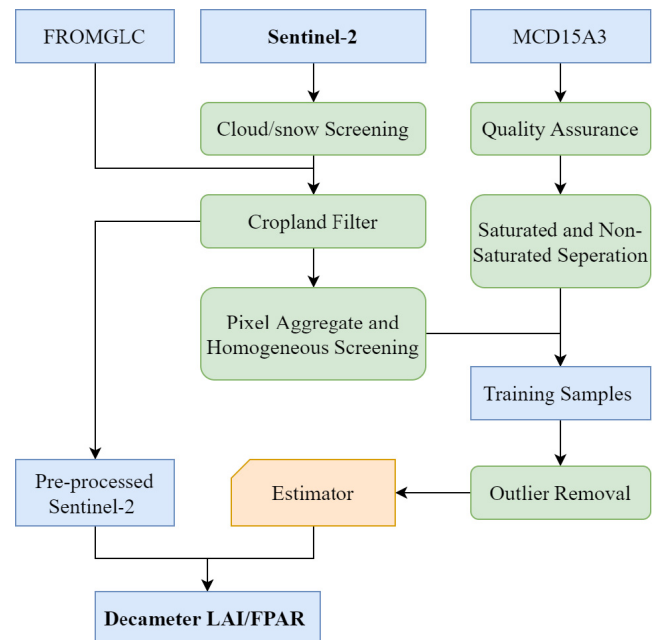


Fig. 2. Flowchart of Sentinel-2 LAI/FPAR retrieval with RF on GEE.

contaminated pixels including cloud, snow, and other high reflected surface. Cloud pixels are removed first using the cloud mask provided by Sentinel-2 L2A original data set. For snow cover and high reflected bare land surface that often appears in the winter and early spring, we recognize them following the criteria that the surface reflectance of all visible and near infrared (VNIR) bands of 10-m resolution, that is, 490, 560, 665, and 842 nm, are greater than 0.3 based on multiple tests for an optimal reflectance threshold to distinguish them. In this manner, some residual cloud pixels that are failed to filter by cloud mask could be further removed either. FROM-GLC10 cropland mask is then applied to the cloud- and snow-free Sentinel-2 image, and only cropland Sentinel-2 pixels are retained.

During the training samples generating process, the cropland masked Sentinel-2 images are then spatially aggregated to a 500-m resolution to match the MODIS data based on the simple average method. Besides the mean value, standard deviation and coefficient of variation are also calculated for each aggregated 500-m pixel. The coefficient of variation is derived as standard variation normalized by the mean value, which represents the reflectance heterogeneity within an aggregated 500-m Sentinel-2 pixel. If the coefficient of variation is greater than 0.1 for any spectral band in green (560 nm), red (665 nm), or near-infrared (842 nm), this 500-m pixel is abandoned because of its high spatial heterogeneity that may cause large uncertainty for reflectance-LAI/FPAR relationship at different scales. The landscape spatial heterogeneity influences the nonlinear estimation of LAI from moderate spatial resolution remote sensing data [30]–[32]. To transfer the 500-m reflectance-LAI/FPAR relationship to 10/20-m spatial scale, all the training samples are generated on an extremely homogenous cropland.

At the same time, the 10-m resolution FROM-GLC10 cropland mask is also spatially aggregated to 500-m resolution. For this binary map, a pixel of 500-m resolution is regarded as

cropland only if at least 90% of its subpixels (i.e., 2250 out of 2500 for 10-m subpixel) are classified as cropland category. Finally, 500-m aggregated Sentinel-2 images are further refined by the 500-m cropland map.

B. MODIS Pixels Screening

We use the ancillary quality-control (QC) labels of each pixel provided by the MODIS LAI/FPAR product to determine the best-quality pixels. Only pixels generated by the main algorithm with or without saturation are retained, and its saturation status is also recorded for further analysis. The MODIS LAI/FPAR is then reprojected from the Sinusoidal to the WGS-84 coordinate to match the processed 500-m Sentinel-2 data.

C. Training Samples Generation

MODIS LAI/FPAR product chooses the maximum estimation within its four-day composite period [28]. We here assume that the vegetation status (i.e., LAI and FPAR values) does not change within a four-day period, thus the Sentinel-2 transits within that period capture the same LAI/FPAR as MODIS dose. Since the temporal resolution of Sentinel-2 is five days combining Sentinel-2A and 2B, there is one Sentinel-2 image at most during a MODIS composite period, and as such, we link the 500-m Sentinel-2 image to 500-m MODIS LAI/FPAR.

Synchronized and overlapped Sentinel-2 and MODIS LAI/FPAR observations are randomly collected within our study area in cropland pixels during a MODIS composite period, and we repeat the sample collecting process throughout the entire year from 2019 to 2020. A total of 95 000 training data pairs are collected at first. Because very few samples are labeled as saturation in MODIS LAI/FPAR quality flag, we further collect 5000 samples in LAI/FPAR saturation pixels. As such, there are 100 000 collected training samples, which are fully spatial and temporal representatives over the study area.

However, the nonsaturation samples are lognormally distributed and concentrated in small LAIs, that is, $\text{LAI} < 1$, thus the training samples are much weighted on sparsely vegetated condition (Fig. 3). Moderate-to-dense vegetated condition is what we especially concern about for better retrieval accuracy. As such, a truncated Gauss distribution restriction in LAI is applied on nonsaturation samples to abandon many small LAI samples (Fig. 3).

We then group the samples based on their LAI and FPAR, and the LAI and FPAR group intervals are 0.5 and 0.1, respectively. Samples whose green (560 nm), red (665 nm), and NIR (842 nm) surface reflectance fall outside of the 1.5 interquartile range (IQR) at each LAI or FPAR interval are removed. IQR is defined as the difference between the 25th and 75th percentiles, which is a measure of data variability. Outliers may come from geo-registration error, aerosol contamination, or incorrect cropland classification, which affect the model performance. Such uncertainties can be reduced to a certain extent after the outliers' removal. The distributions of green, red, and NIR surface reflectance of Sentinel-2 of training

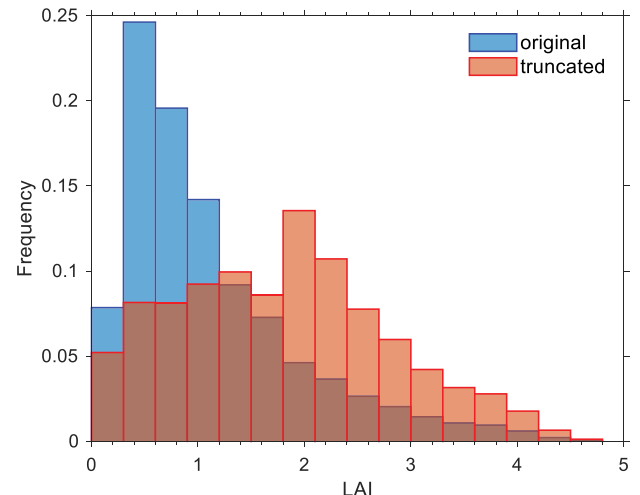


Fig. 3. LAI frequency histograms of nonsaturation samples before and after truncated Gauss distribution restriction.

samples over different LAI or FPAR intervals are demonstrated in Fig. 4. The green and red reflectance decreases while the NIR reflectance increases as the LAI or FPAR increases. Note that when the LAI group number is greater than 5 or 6, that is $\text{LAI} > 2.5$, the reflectance of green, red, and NIR gets saturated and their uncertainty rises (Fig. 4). There are 46 963 nonsaturation and 10 355 saturation training samples left, respectively, in the end.

D. LAI/FPAR Inversion Using RF Model

A wide variety of machine learning models are proposed for regression and function approximation. This study employed the RF model to retrieve LAI and FPAR from the processed Sentinel-2 surface reflectance data. An RF is a combination of multiple classifications and regression trees (CARTs), and each of them is trained by different subsets of features and examples [33]. The output of an RF is the mean prediction of the individual trees. Like bagging, multiple subsample sets are sampled from the original training set with bootstrap sampling, and each CART is trained with a subsample set. Instead of using all the features, a random selection of features is used to split each node during the construction of each CART. The main advantage of using RF over other traditional machine learning algorithms such as a neural network (NN) is that it can cope with high dimensional problems easily, thanks to its pruning strategy. In addition, unlike kernel methods, RF is more computationally efficient. Thus, it has been applied in many parameter retrieval applications in the remote sensing community, such as LAI, leaf chlorophyll content, and solar-induced chlorophyll fluorescence [21], [33], [34].

The RF regressor is trained using the LAI/FPAR from MODIS and the processed Sentinel-2 surface multiple-band reflectance and its corresponding sun-sensor geometry. Two sets of training inputs are employed in this study: the first group (10-m inputs hereafter) is the reflectance of 10-m resolution, which includes green (560 nm), red (665 nm), and NIR (842 nm) bands, together with the normalized sun-sensor geometry, which is the absolute cosine of solar zenith angle (SZA), view zenith angle (VZA), and relative

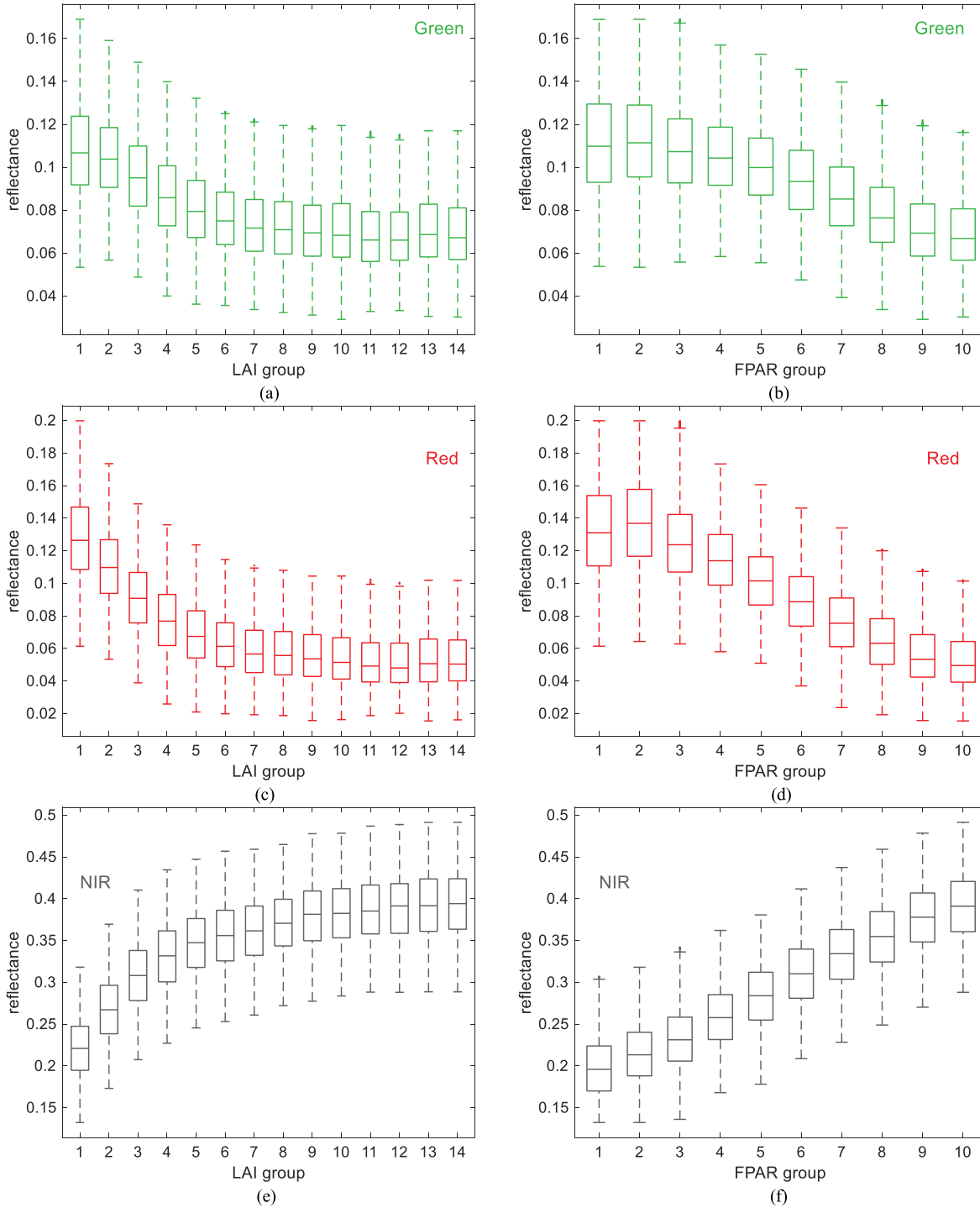


Fig. 4. Whisker boxplots of green (560 nm), red (665 nm), and NIR (842 nm) surface reflectance for different LAIs or FPARs. The boxes and whiskers indicate the minimum, 25th, 50th, and 75th percentiles and maximum reflectance of a group. The interval of LAI is 0.5 from 0 to 7 for the group 1 to group 14, and the interval of FPAR is 0.1 from 0 to 1 for the group 1 to 10. (a) Green band under LAI groups. (b) Green band under FPAR groups. (c) Red band under LAI groups. (d) Red band under FPAR groups. (e) NIR band under LAI groups. (f) NIR band under FPAR groups.

azimuth angle (RAA). Blue (490 nm) band is not used because it is most sensitive to atmospheric scattering effects, which leads to high uncertainty [35], [36]. The other group (20-m inputs hereafter) employs the reflectance of both 10- (green, red, and NIR) and 20-m resolution including RE1 (705 nm), RE2 (740 nm), RE3 (783 nm), SWIR1 (1610 nm), and SWIR2 (2190 nm). The outputs of the RF model are LAI and FPAR

values. During the RF training process, the number of RF trees is set as 50 and the minimum leaf population is set as 3. The models are trained with nonsaturation samples, saturation samples and all samples, respectively. The training data set is composed of 70% of all samples, which are selected from saturation and nonsaturation data set proportionally, while the remaining 30% samples are regarded as the test data set.

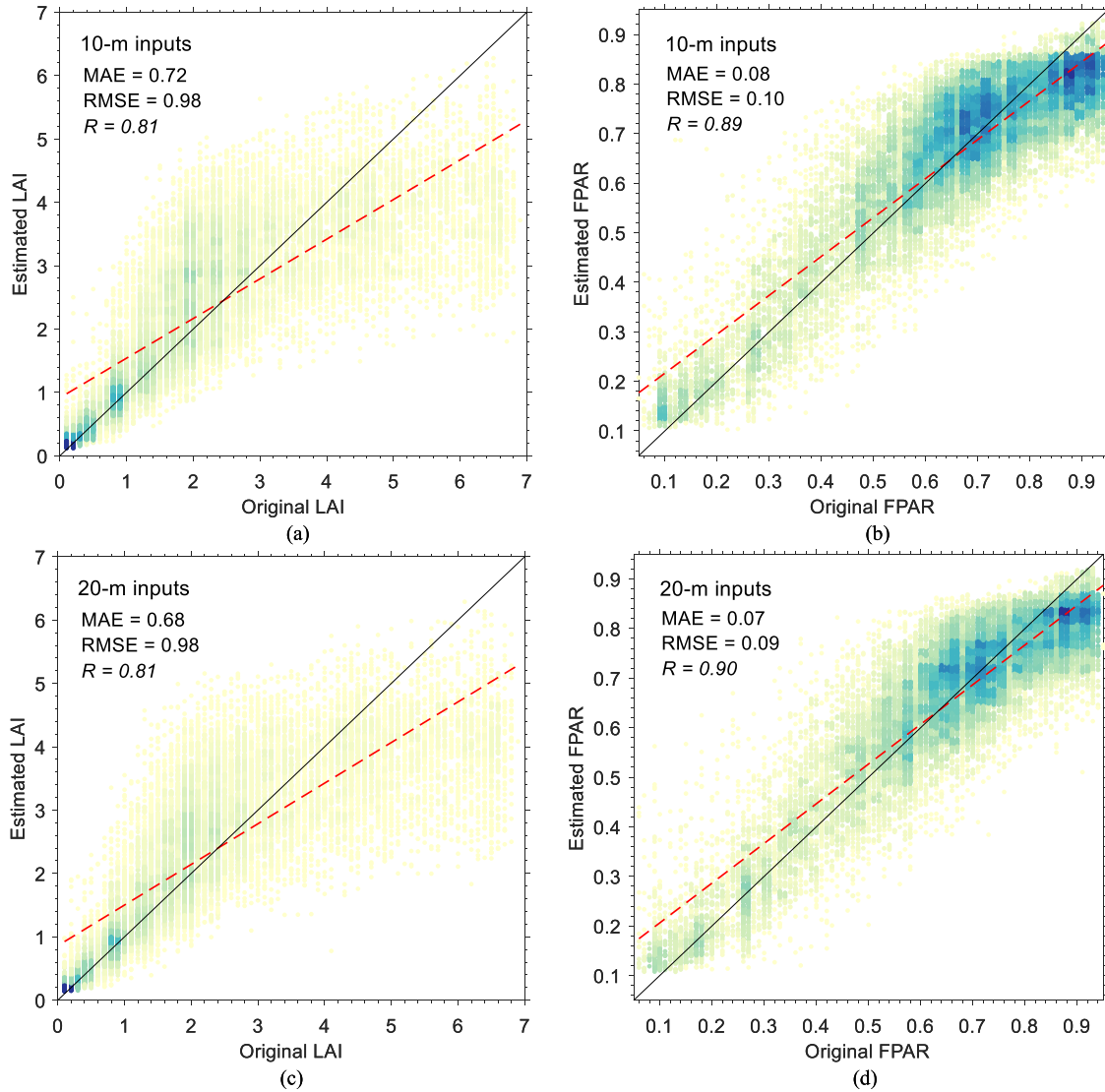


Fig. 5. Scatterplot of original LAI/FPAR and estimated LAI/FPAR from the RF model with 10-m inputs and 20-m inputs on test data sets. (a) LAI with 10-m inputs. (b) FPAR with 10-m inputs. (c) LAI with 20-m inputs. (d) FPAR with 20-m inputs.

TABLE II
ACCURACY METRICS OF LAI RETRIEVAL ON TEST DATA SET

	MAE		RMSE		R	
	10 m	20 m	10 m	20 m	10 m	20 m
Non-saturation	0.40	0.39	0.55	0.83	0.83	0.84
Saturation	0.72	0.71	0.83	0.82	0.20	0.22
All	0.72	0.68	1.02	0.98	0.79	0.81

IV. COMPARISON AND VALIDATION

A. Model Theoretical Performance

In this section, we will evaluate the performance of the RF model for LAI/FPAR retrieval on the test data set. The mean absolute error (MAE), RMSE, and Person's correlation coefficient (R) are adopted as accuracy metrics to assess the results quantitatively.

Table II, Fig. 5(a) and (c) show the accuracy results of LAI retrieval on the test data set. The RF model trained with nonsaturation samples has a better performance in absolute accuracy indicators (MAE = 0.40 and RMSE = 0.55 for 10-m inputs) than with saturation samples (MAE = 0.72 and

RMSE = 0.83 for 10-m inputs), and the model trained with all samples without saturation and nonsaturation separation achieves the poorest performance (MAE = 0.72 and RMSE = 1.02 for 10-m inputs). Model trained on saturation samples exhibits a small correlation coefficient ($R = 0.20$ for 10-m inputs), indicating the spectral saturation issue in densely vegetated condition greatly influence the model performance. By adding red-edge (RE) and SWIR information of Sentinel-2 as inputs, the retrieval performance improves for all vegetated conditions, which demonstrates the value of RE and/or SWIR in LAI estimation [37]–[39]. The overall performance is almost unbiased (Fig. 6), but it should be noted that under- or over-estimation happens for different LAI conditions. The LAI result is slightly overestimated in the LAI interval of 1–3, while it turns to be greatly underestimated when LAI is greater than 4 (Figs. 5 and 7).

The accuracy results of FPAR retrieval on training and test data set are shown in Table III, Fig. 5(b) and (d). FPAR retrieval model trained with saturation samples achieves the best performance (MAE = 0.03 and RMSE = 0.03 for 10-m inputs) compared with models on nonsaturation samples,

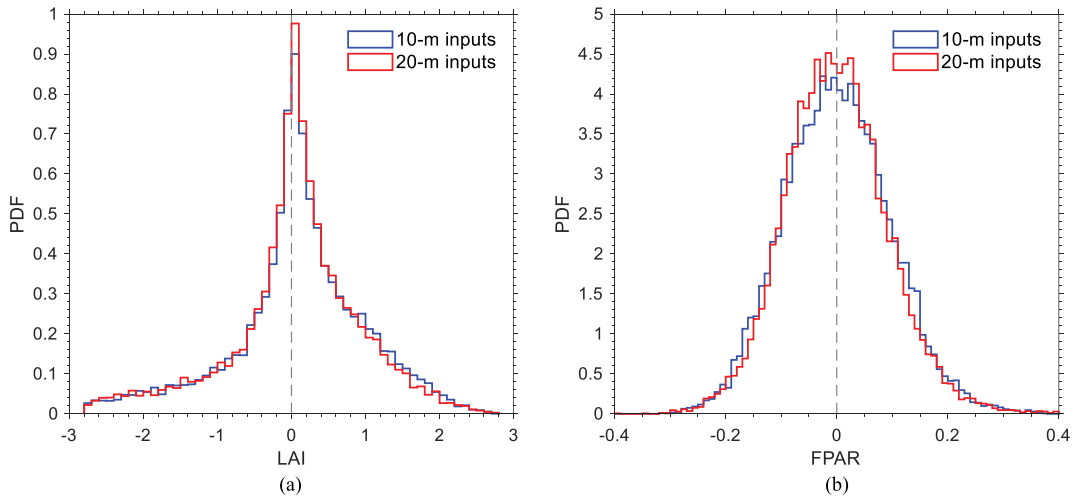


Fig. 6. Histogram of the difference between estimated LAI/FPAR and original LAI/FPAR. (a) LAI. (b) FPAR.

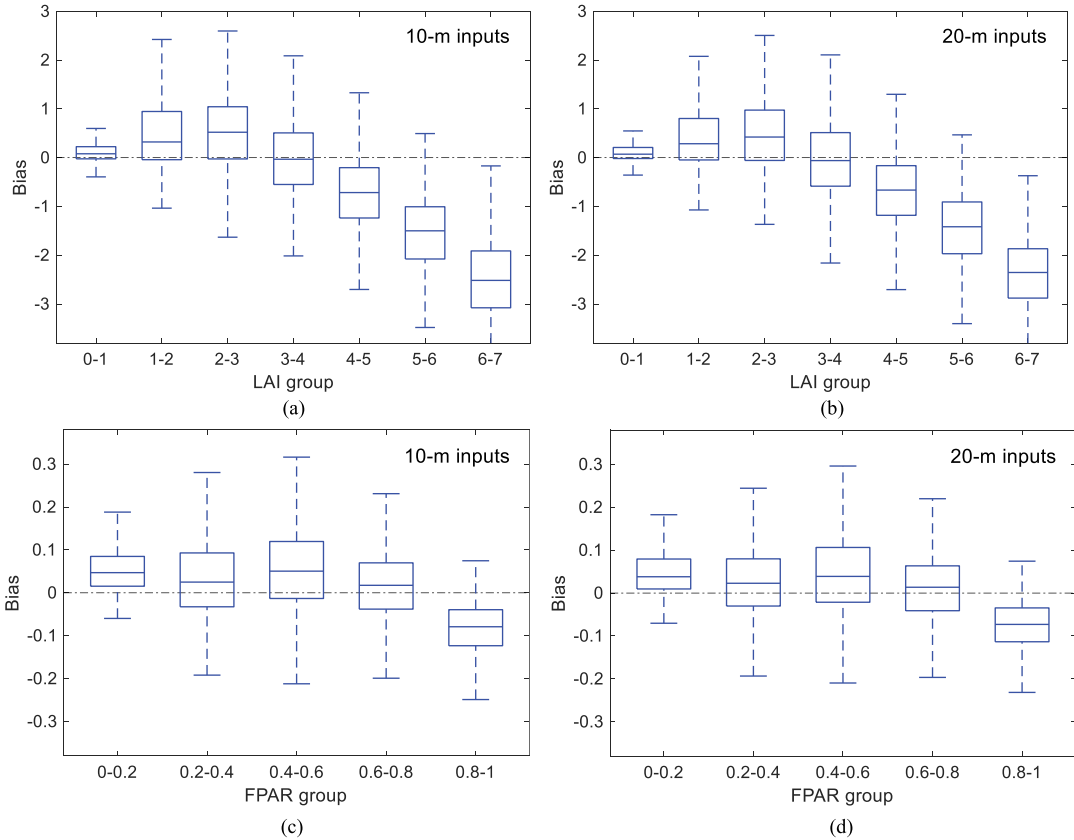


Fig. 7. Whisker boxplots of LAI/FPAR estimation bias for different LAIs and FPARs. (a) LAI with 10-m inputs. (b) LAI with 20-m inputs. (c) FPAR with 10-m inputs. (d) FPAR with 20-m inputs.

TABLE III
ACCURACY METRICS OF FPAR RETRIEVAL ON TEST DATA SET

	MAE		RMSE		R	
	10 m	20 m	10 m	20 m	10 m	20 m
Non-saturation	0.07	0.07	0.09	0.09	0.89	0.89
Saturation	0.03	0.03	0.03	0.03	0.22	0.18
All	0.08	0.07	0.10	0.09	0.89	0.90

which is very different from that of LAI. This is because the variation of saturated FPAR is much smaller than that of saturated LAI, and the saturation issue of spectral reflectance

affects greater on LAI than on FPAR. The accuracy of models on nonsaturation samples and all samples are similar, indicating the separation of saturation and nonsaturation samples is not necessary for FPAR retrieval. The proposed RF model has a better performance on FPAR than on LAI since the correlation coefficient between estimated FPAR and its truth value ($R = 0.89$ for all samples 10-m inputs on training data set) is higher than that of LAI. Besides, the extra input information from RE and SWIR also slightly improves the FPAR estimation performance. The overall performance is also unbiased for FPAR (Fig. 6),

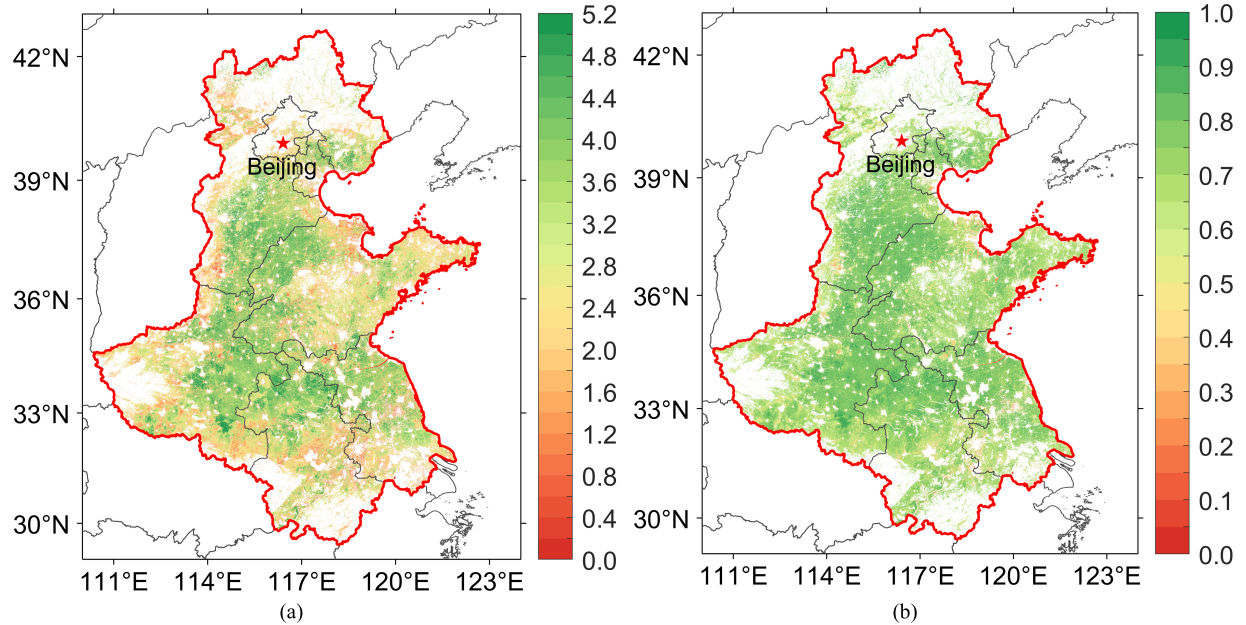


Fig. 8. Monthly composite of LAI and FPAR map over Northern China plain in August 2019 from Sentinel-2 20-m inputs. (a) LAI. (b) FPAR.

and slight underestimation is observed for FPAR greater than 0.8 (Figs. 5 and 7).

B. Intercomparing With MODIS Product

In Section IV-A, we evaluated the performance of the models on high-quality test samples. In this section, the proposed LAI/FPAR retrieval models are applied on real Sentinel-2 images for a further intercomparing with MODIS product. Because the saturation indicator on Sentinel-2 pixel is not available, thus the models trained with all samples are used afterward. The link of a toy example of the code is provided in Appendix.

Fig. 8 shows the monthly composite LAI and FPAR map over Northern China plain in August 2019 derived based on our method from Sentinel-2 20-m inputs. We then select a small cropland region near Hengshui City centered at 115.5° E, 38.0° N in the center of our study area, which covers $\sim 2000 \text{ km}^2$, for Sentinel-2 and MODIS LAI/FPAR detailed comparison. According to the phenology of wheat and maize cultivated in this region, the LAI and FPAR derived in early April (green-recovering stage of wheat) and late August (grain-filling stage of maize) are chosen as the representative of sparse-to-moderate vegetated condition and dense vegetation condition.

Fig. 9(a)–(f) illustrates the comparison of Sentinel-2 and MODIS LAI maps in April and August of 2019. The spatial distribution of Sentinel-2 LAI and MODIS LAI is consistent both in April and in August, but the Sentinel-2 results provide more spatial details compared with that of MODIS. The average LAI is about 1.6 and 4.4 over this region for April and August, respectively. Fig. 9(g) and (h) suggest the quantitative difference between LAI from Sentinel-2 and MODIS. The Sentinel-2 LAI is aggregated to 500-m resolution using the arithmetical average method. In the sparse-to-moderate vegetated condition [early April, Fig. 9(a)–(c)], the retrieval

performance is much better than that in the densely vegetated condition (late August, Fig. 9(d)–(f)], with MAE of 0.27 and 0.91 for April and August with 10-m inputs, respectively. Models with 20-m inputs show a higher retrieval accuracy compared with that of 10-m inputs in densely vegetated conditions. Besides, 10-m inputs model is slightly overestimated especially in sparse-to-moderate vegetated condition, while 20-m inputs model rectifies the bias.

Fig. 10(a)–(f) shows the comparison of Sentinel-2 and MODIS FPAR maps in April and August of 2019. Spatial consistency could still be observed between Sentinel-2 FPAR and MODIS FPAR, with more spatial details in Sentinel-2 results. The average FPAR is about 0.4 and 0.85 over this region for April and August, respectively. Fig. 10(g) and (h) quantifies the difference between FPAR from Sentinel-2 and MODIS. The retrieval accuracy is similar in the sparse-to-moderate vegetated condition (early April, Fig. 10(a)–(c)] and the dense vegetated condition [late August, Fig. 10(d)–(f)]. In sparse-to-moderate vegetated condition, FPAR estimation is overestimated either for 10-m inputs model or 20-m inputs model, but the degree of overestimation much declines for 20-m inputs model. In dense vegetated condition, the FPAR retrieval accuracies are similar for two group of inputs.

Note that dual peaks appear in LAI histograms of August, and it may cause by a two-day delay of Sentinel-2 imaging date compared with that of MODIS. Besides, the MODIS LAI saturation issue in densely vegetated condition may be another source of this discrepancy [29].

Three homogeneous cropland sites located at Hengshui (115.51° E, 37.88° N), Luohe (113.11° E, 33.69° N) and Xiaotangshan (116.44° E, 40.18° N) across the study area are selected to check the temporal variation of the Sentinel-2 LAI/FPAR results. Fig. 11 shows the temporal LAI/FPAR trajectories over these three sites for the entire year of 2019. For a better comparison, Sentinel-2 results are aggregated to

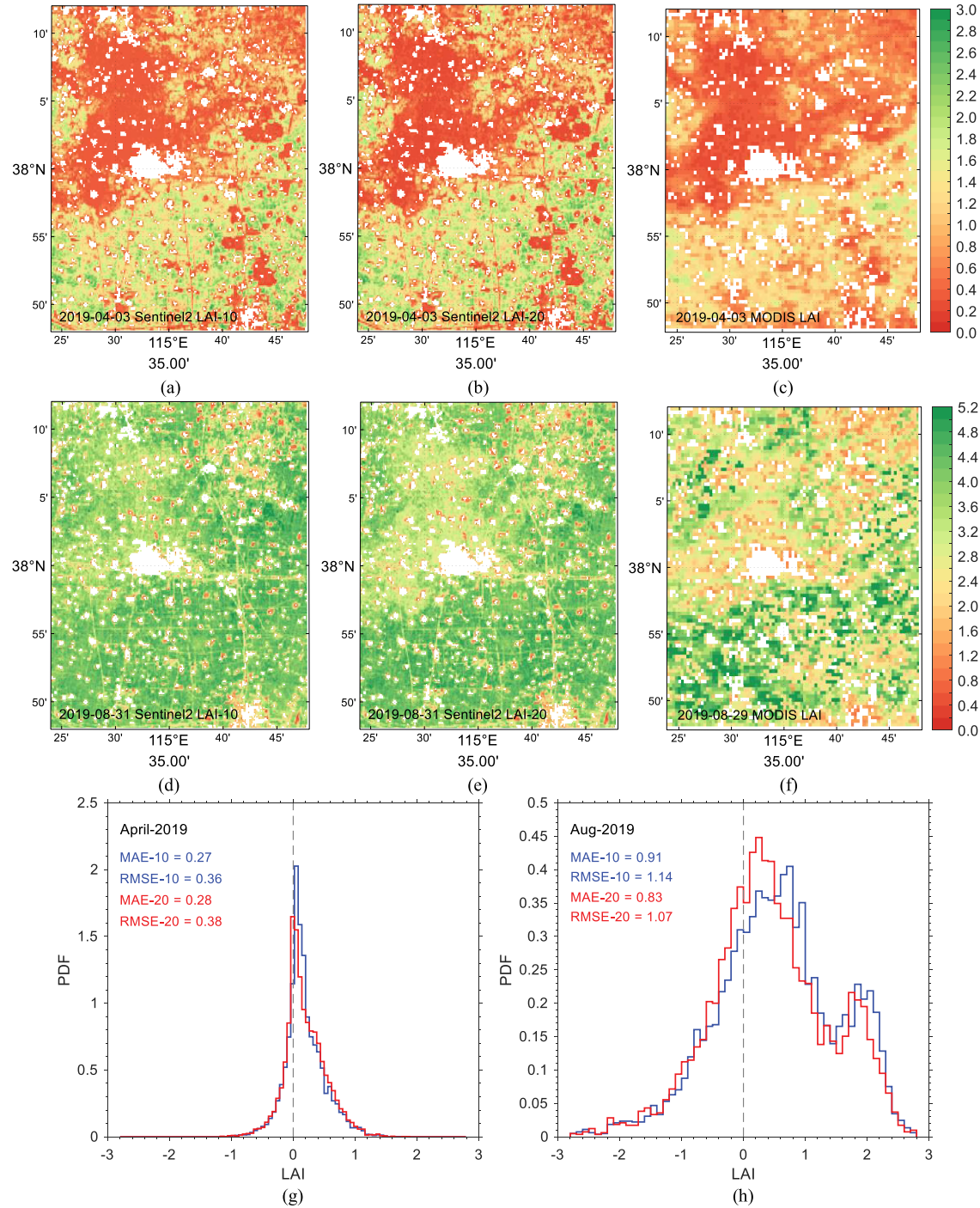


Fig. 9. LAI maps and histograms of LAI difference of a small cropland region near Hengshui City derived from Sentinel-2 and MODIS on early April and late August of 2019. Histograms of the difference are calculated between Sentinel-2 LAI and MODIS LAI for early April and late August. (a) 10-m LAI from Sentinel-2 in April. (b) 20-m LAI from Sentinel-2 in April. (c) 500-m LAI from MODIS in April. (d) 10-m LAI from Sentinel-2 in August. (e) 20-m LAI from Sentinel-2 in August. (f) 500-m LAI from MODIS in August. (g) Histograms of LAI difference in April. (h) Histograms of LAI difference in August.

500 m to match the MODIS resolution. The bimodal pattern of LAI and FPAR seasonality over these sites is caused by rotation agricultural management of wheat and maize during a year, and the peak of wheat growing appears in April to May and maize in August to September, depending on the site's latitude. The Sentinel-2 and MODIS LAI/FPAR are in good agreement in the entire year for all these three sites, while few

mismatches only happen in the extreme high or low vegetation condition.

C. Ground Validation

Ground LAI observations are used to directly validate the accuracy of the Sentinel-2 LAI retrieval result. The LAI *in situ* observations is collected near Hengshui and

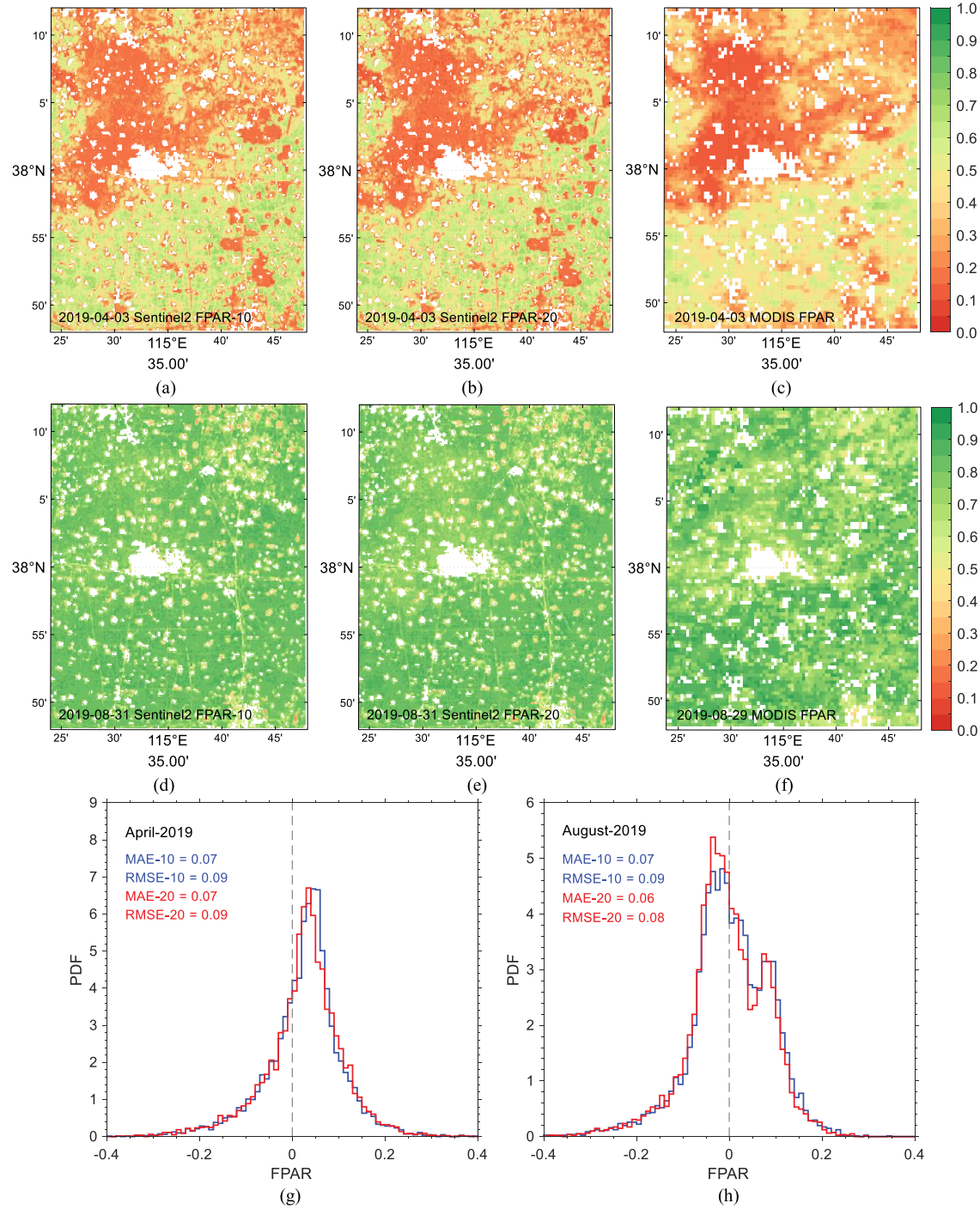


Fig. 10. FPAR maps and histograms of FPAR difference of a small cropland region near Hengshui City derived from Sentinel-2 and MODIS on early April and late August of 2019. Histograms of the difference are calculated between Sentinel-2 FPAR and MODIS FPAR for early April and late August. (a) 10-m FPAR from Sentinel-2 in April. (b) 20-m FPAR from Sentinel-2 in April. (c) 500-m FPAR from MODIS in April. (d) 10-m FPAR from Sentinel-2 in August. (e) 20-m FPAR from Sentinel-2 in August. (f) 500-m FPAR from MODIS in August. (g) Histograms of FPAR difference in April. (h) Histograms of FPAR difference in August.

Luohe experimental sites mentioned in Section IV-B during the wheat growing seasons of 2017 and 2018. The LAI was measured using an LAI-2000 Plant Canopy Analyzer (Li-Cor Inc., Lincoln, NE, USA) in a homogeneous cropland elementary sampling unit (ESU) of 10 m × 10 m, and a total of 40 LAI measurements were collected.

Fig. 12 shows the ground validation result of Sentinel-2 LAI maps. A good agreement between the ground-measured LAI and retrieved LAI from Sentinel-2 data are observed for 10- and 20-m inputs models, but the 20-m LAI values are in slight better agreement with the ground measurements (MAE = 0.62 and RMSE = 0.72) than the 10-m LAI values (MAE = 0.73 and RMSE = 0.83).

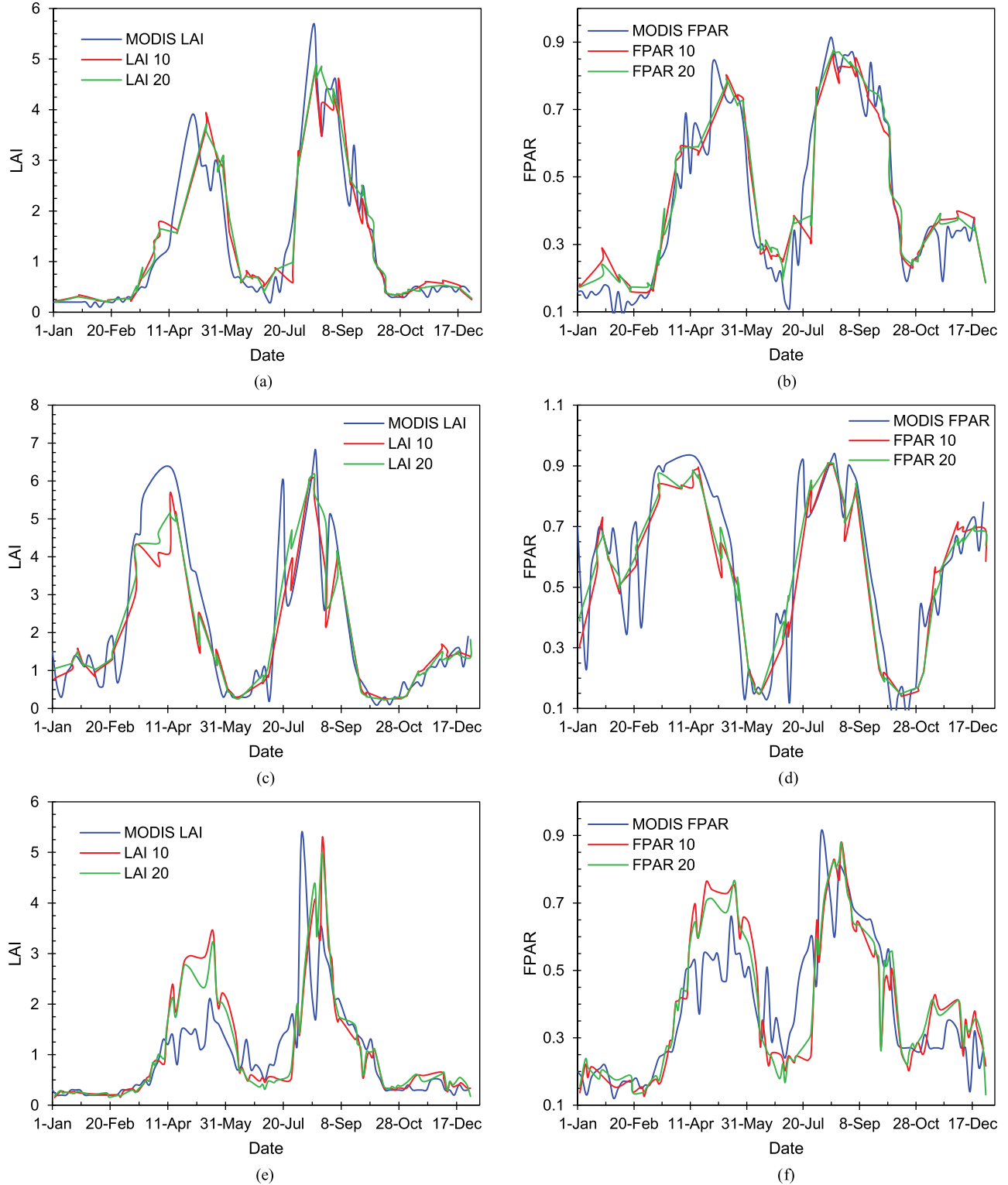


Fig. 11. Yearly variation in 2019 of LAI/FPAR time series from Sentinel-2 and MODIS over Hengshui, Luohe and Xiaotangshan cropland sites. (a) Hengshui LAI. (b) Hengshui FPAR. (c) Luohe LAI. (d) Luohe FPAR. (e) Xiaotangshan LAI. (f) Xiaotangshan FPAR.

V. DISCUSSION

Timely retrieving high spatial and temporal resolution vegetation variables of crop from optical remotely sensed data is of great importance for agricultural management [2], and it is still a challenging task due to the issues in data acquisition, model accuracy, and massive computational time-consuming. This

article proposed a decameter cropland LAI/FPAR retrieval framework from Sentinel-2 surface reflectance data on the GEE platform for Northern China plain, and the performance of the methods is generally acceptable based on the inter-comparisons and ground validations. Nevertheless, the method could still be improved in accuracy and practicability.

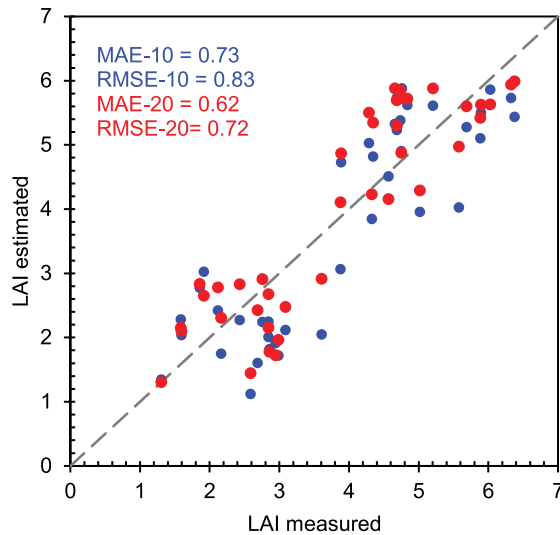


Fig. 12. Comparison of Sentinel-2 derived LAI with ground-measured LAI.

Spectral saturation happens in densely vegetated condition greatly affects the retrieval accuracy especially for LAI [6], [40], [41]. The introduction of RE and SWIR information of Sentinel-2 slightly improved the model performance, and it is consistent with the conclusion of many related literature studies [37]–[39]. The retrieval accuracy has remarkably improved when the saturation and nonsaturation samples are separated in model training process, which indicates that the pixel saturation flag is an influential factor for LAI/FPAR retrieval. Thus, it is expectable to improve the overall estimation accuracy if the pixel saturation flag could be obtained, e.g., by using an advanced machine learning algorithm in high-dimensional spectral space.

The residual cloud and aerosol contamination after atmospheric correction is another source of uncertainty of the LAI/FPAR retrieval results [42]. Even though the samples used for training are strictly filtered by cloud mask and 1.5 IQR criteria mentioned in Section III-C, some bad-quality samples still exist, which undermines the model performance. On the other hand, even if the retrieval model is built on hundred percent high-quality samples, the realistic pixel to be estimated is somewhat influenced by aerosol effect, which could not be completely removed by atmospheric correction, and those pixels with high aerosol optical depth (AOD) will obviously result in retrieval failure based on our algorithm built in small or no aerosol condition.

Other factors, such as the uncertainty of the MODIS LAI/FPAR product and landcover product, also affect the retrieval accuracy and model performance [43], [44]. The cropland mask data set from FROM-GLC adopted in this study was generated in 2017, and we have assumed that the land cover and land use did not change during the period of 2017–2020. However, the land cover cropland distribution is dynamic from year to year; therefore, an annual dynamic land cover product is necessary for a more accurate application.

Although the RF model is robust and efficient enough to deal with this high dimensional parameters’ retrieval task, more advanced machine learning algorithms, such as deep learning methods, may further exploit the spectral and spatial/temporal information and achieve better performance [45]–[47]. Moreover, standardized ten-day or monthly composite high-resolution cropland LAI/FPAR product with no gap may be more useful and essential for continues operational agricultural monitoring applications; hence, image composition and missing data recovery technics will be adopted to obtain standardized product in the forthcoming investigation [48]–[50]. Besides, a harmonized Sentinel-2 and Landsat data set can further improve the temporal resolution of decameter cropland LAI/FPAR product [51].

VI. CONCLUSION

A method of retrieving decameter cropland LAI/FPAR from Sentinel-2 surface reflectance data using the RF model on the GEE platform over Northern China plain is developed in this study, which is beneficial for monitoring crop growth and large-scale drought. The RF model is first trained using the spatial aggregated Sentinel-2 surface reflectance on homogeneous cropland and the corresponding MODIS LAI/FPAR product. There are two groups of band reflectance inputs, one is 10-m inputs, which include the surface reflectance of Sentinel-2 10-m resolution bands, that is green, red, and NIR and sun-senor geometry (called 10-m inputs), and the other is Sentinel-2 20-m resolution bands together with 10-m band, which adds RE1, RE2, RE3, SWIR1, and SWIR2 (called 20-m inputs). The outputs of the RF model are LAI and FPAR. The results demonstrated that both 10-m inputs RF model and 20-m inputs RF model can estimate LAI/FPAR appropriately, and the model theoretical performance showed that 20-m inputs RF model had better accuracy for both LAI and FPAR retrieval. The new method was used to retrieve LAI/FPAR from Sentinel-2 image, and the retrieved LAI/FPAR was then compared with the MODIS LAI/FPAR product, getting consistent distribution with MODIS spatially and temporally. The histogram of Sentinel-2 20-m LAI/FPAR agreed somewhat better with the MODIS than Sentinel-2 10-m LAI/FPAR especially in sparse-to-moderate vegetated condition, while the latter showed a slight overestimation. Direct validation with ground LAI measurements also indicated that the accuracy of the Sentinel-2 20-m result was better than that of 10-m result. Spectral saturation, aerosol and cloud contamination, and uncertainty of MODIS LAI/FPAR and land cover products could be the sources of uncertainty in decameter LAI/FPAR result; thus, it should be addressed in the further work. Moreover, the new retrieval method can also be applied to other high-resolution sensors such as Landsat OLI or ETM+, and further considerations of the retrieval of LAI/FPAR from harmonized Sentinel-2 and Landsat data will be explored in a forthcoming study.

APPENDIX

An example of the code is available at <https://code.earthengine.google.com/6f84a4a76edd6952392784cff5ced93a>.

REFERENCES

- [1] R. Vos and L. G. Bellù, "Global trends and challenges to food and agriculture into the 21st century," in *Sustainable Food and Agriculture*, C. Campanhola and S. Pandey Eds. New York, NY, USA: Academic, 2019, ch. 2, pp. 11–30.
- [2] M. Weiss, F. Jacob, and G. Duveiller, "Remote sensing for agricultural applications: A meta-review," *Remote Sens. Environ.*, vol. 236, Jan. 2020, Art. no. 111402, doi: [10.1016/j.rse.2019.111402](https://doi.org/10.1016/j.rse.2019.111402).
- [3] J. M. Chen and T. A. Black, "Defining leaf area index for non-flat leaves," *Plant, Cell Environ.*, vol. 15, no. 4, pp. 421–429, May 1992, doi: [10.1111/j.1365-3040.1992.tb00992.x](https://doi.org/10.1111/j.1365-3040.1992.tb00992.x).
- [4] I. Alados, I. Foye-Moreno, and L. Alados-Arboledas, "Photosynthetically active radiation: Measurements and modelling," *Agricul. Forest Meteorol.*, vol. 78, no. 1, pp. 121–131, Jan. 1996, doi: [10.1016/0168-1923\(95\)02245-7](https://doi.org/10.1016/0168-1923(95)02245-7).
- [5] Y. Knyazikhin, J. V. Martonchik, R. B. Myneni, D. J. Diner, and S. W. Running, "Synergistic algorithm for estimating vegetation canopy leaf area index and fraction of absorbed photosynthetically active radiation from MODIS and MISR data," *J. Geophys. Res., Atmos.*, vol. 103, no. D24, pp. 32257–32275, Dec. 1998, doi: [10.1029/98jd02462](https://doi.org/10.1029/98jd02462).
- [6] H. Fang, F. Baret, S. Plummer, and G. Schaepman-Strub, "An overview of global leaf area index (LAI): Methods, products, validation, and applications," *Rev. Geophys.*, vol. 57, no. 3, pp. 739–799, Sep. 2019, doi: [10.1029/2018rg000608](https://doi.org/10.1029/2018rg000608).
- [7] A. A. Gitelson, "Wide dynamic range vegetation index for remote quantification of biophysical characteristics of vegetation," *J. Plant Physiol.*, vol. 161, no. 2, pp. 165–173, Jan. 2004, doi: [10.1017/0176-1617-01176](https://doi.org/10.1017/0176-1617-01176).
- [8] Y. Fei *et al.*, "Comparison of different methods for corn LAI estimation over Northeastern China," *Int. J. Appl. Earth Observ. Geoinf.*, vol. 18, pp. 462–471, Aug. 2012, doi: [10.1016/j.jag.2011.09.004](https://doi.org/10.1016/j.jag.2011.09.004).
- [9] J. Sui *et al.*, "Winter wheat production estimation based on environmental stress factors from satellite observations," *Remote Sens.*, vol. 10, no. 6, p. 962, Jun. 2018, doi: [10.3390/rs10060962](https://doi.org/10.3390/rs10060962).
- [10] W. Wang *et al.*, "An interplay between photons, canopy structure, and recollision probability: A review of the spectral invariants theory of 3D canopy radiative transfer processes," *Remote Sens.*, vol. 10, no. 11, p. 1805, Nov. 2018, doi: [10.3390/rs10111805](https://doi.org/10.3390/rs10111805).
- [11] K. Yan *et al.*, "Evaluation of MODIS LAI/FPAR product collection 6. Part 1: Consistency and improvements," *Remote Sens.*, vol. 8, no. 5, p. 359, Apr. 2016. [Online]. Available: <https://www.mdpi.com/2072-4292/8/5/359>
- [12] B. Yang *et al.*, "Estimation of leaf area index and its sunlit portion from DSCOVR EPIC data: Theoretical basis," *Remote Sens. Environ.*, vol. 198, pp. 69–84, Sep. 2017, doi: [10.1016/j.rse.2017.05.033](https://doi.org/10.1016/j.rse.2017.05.033).
- [13] F. Baret *et al.*, "GEOV1: LAI and FPAR essential climate variables and FCOVER global time series capitalizing over existing products. Part1: Principles of development and production," *Remote Sens. Environ.*, vol. 137, pp. 299–309, Oct. 2013, doi: [10.1016/j.rse.2012.12.027](https://doi.org/10.1016/j.rse.2012.12.027).
- [14] F. J. García-Haro *et al.*, "Derivation of global vegetation biophysical parameters from EUMETSAT polar system," *ISPRS J. Photogramm. Remote Sens.*, vol. 139, pp. 57–74, May 2018, doi: [10.1016/j.isprsjprs.2018.03.005](https://doi.org/10.1016/j.isprsjprs.2018.03.005).
- [15] F. Baret *et al.*, "LAI, FPAR and fCover CYCLOPES global products derived from VEGETATION: Part 1: Principles of the algorithm," *Remote Sens. Environ.*, vol. 110, no. 3, pp. 275–286, Oct. 2007, doi: [10.1016/j.rse.2007.02.018](https://doi.org/10.1016/j.rse.2007.02.018).
- [16] M. Drusch *et al.*, "Sentinel-2: ESA's optical high-resolution mission for GMES operational services," *Remote Sens. Environ.*, vol. 120, pp. 25–36, May 2012, doi: [10.1016/j.rse.2011.11.026](https://doi.org/10.1016/j.rse.2011.11.026).
- [17] Q. Hu *et al.*, "Evaluation of global decametric-resolution LAI, FPAR and FVC estimates derived from Sentinel-2 imagery," *Remote Sens.*, vol. 12, no. 6, p. 912, Mar. 2020. [Online]. Available: <https://www.mdpi.com/2072-4292/12/6/912>
- [18] N. Gorelick, M. Hancher, M. Dixon, S. Ilyushchenko, D. Thau, and R. Moore, "Google Earth engine: Planetary-scale geospatial analysis for everyone," *Remote Sens. Environ.*, vol. 202, pp. 18–27, Dec. 2017, doi: [10.1016/j.rse.2017.06.031](https://doi.org/10.1016/j.rse.2017.06.031).
- [19] Y. H. Tsai, D. Stow, L. An, H. L. Chen, R. Lewison, and L. Shi, "Monitoring land-cover and land-use dynamics in fanjingshan national nature reserve," *Appl. Geography*, vol. 111, Oct. 2019, Art. no. 102077, doi: [10.1016/j.apgeog.2019.102077](https://doi.org/10.1016/j.apgeog.2019.102077).
- [20] H. Tian, N. Huang, Z. Niu, Y. Qin, J. Pei, and J. Wang, "Mapping winter crops in China with multi-source satellite imagery and phenology-based algorithm," *Remote Sens.*, vol. 11, no. 7, p. 820, Apr. 2019, doi: [10.3390/rs11070820](https://doi.org/10.3390/rs11070820).
- [21] M. Campos-Taberner *et al.*, "Global estimation of biophysical variables from Google Earth engine platform," *Remote Sens.*, vol. 10, no. 8, p. 1167, Jul. 2018, doi: [10.3390/rs10081167](https://doi.org/10.3390/rs10081167).
- [22] J. Sun, L. Di, Z. Sun, Y. Shen, and Z. Lai, "County-level soybean yield prediction using deep CNN-LSTM model," *Sensors*, vol. 19, no. 20, p. 4363, Oct. 2019, doi: [10.3390/s19204363](https://doi.org/10.3390/s19204363).
- [23] S. L. Ermida, P. Soares, V. Mantas, F.-M. Götsche, and I. F. Trigo, "Google Earth engine open-source code for land surface temperature estimation from the Landsat series," *Remote Sens.*, vol. 12, no. 9, p. 1471, May 2020.
- [24] M. Mahdianpari, B. Salehi, F. Mohammadimanesh, S. Homayouni, and E. Gill, "The first wetland inventory map of newfoundland at a spatial resolution of 10 m using Sentinel-1 and Sentinel-2 data on the Google Earth engine cloud computing platform," *Remote Sens.*, vol. 11, no. 1, p. 43, Dec. 2018.
- [25] Z. Shao, H. Fu, D. Li, O. Altan, and T. Cheng, "Remote sensing monitoring of multi-scale watersheds impermeability for urban hydrological evaluation," *Remote Sens. Environ.*, vol. 232, Oct. 2019, Art. no. 111338, doi: [10.1016/j.rse.2019.111338](https://doi.org/10.1016/j.rse.2019.111338).
- [26] Y. Zhang *et al.*, "Optimal hyperspectral characteristics determination for winter wheat yield prediction," *Remote Sens.*, vol. 10, no. 12, p. 2015, Dec. 2018, doi: [10.3390/rs10122015](https://doi.org/10.3390/rs10122015).
- [27] P. Gong *et al.*, "Stable classification with limited sample: Transferring a 30-m resolution sample set collected in 2015 to mapping 10-m resolution global land cover in 2017," *Sci. Bull.*, vol. 64, no. 6, pp. 370–373, Mar. 2019, doi: [10.1016/j.scib.2019.03.002](https://doi.org/10.1016/j.scib.2019.03.002).
- [28] R. B. Myneni *et al.*, "Global products of vegetation leaf area and fraction absorbed PAR from year one of MODIS data," *Remote Sens. Environ.*, vol. 83, nos. 1–2, pp. 214–231, Nov. 2002, doi: [10.1016/S0034-4257\(02\)00074-3](https://doi.org/10.1016/S0034-4257(02)00074-3).
- [29] K. Yan *et al.*, "Evaluation of MODIS LAI/FPAR product collection 6. Part 2: Validation and intercomparison," *Remote Sens.*, vol. 8, no. 6, p. 460, May 2016. [Online]. Available: <https://www.mdpi.com/2072-4292/8/6/460>
- [30] S. Garrigues, D. Allard, F. Baret, and M. Weiss, "Influence of landscape spatial heterogeneity on the non-linear estimation of leaf area index from moderate spatial resolution remote sensing data," *Remote Sens. Environ.*, vol. 105, no. 4, pp. 286–298, Dec. 2006, doi: [10.1016/j.rse.2006.07.013](https://doi.org/10.1016/j.rse.2006.07.013).
- [31] G. Yin *et al.*, "Improving leaf area index retrieval over heterogeneous surface by integrating textural and contextual information: A case study in the Heihe river basin," *IEEE Geosci. Remote Sens. Lett.*, vol. 12, no. 2, pp. 359–363, Feb. 2015, doi: [10.1109/lgrs.2014.2341925](https://doi.org/10.1109/lgrs.2014.2341925).
- [32] L. Wu *et al.*, "Scaling correction of remotely sensed leaf area index for farmland landscape pattern with multitype spatial heterogeneities using fractal dimension and contextual parameters," *IEEE J. Sel. Topics Appl. Earth Observ. Remote Sens.*, vol. 11, no. 5, pp. 1472–1481, May 2018, doi: [10.1109/jstars.2018.2799955](https://doi.org/10.1109/jstars.2018.2799955).
- [33] M. Belgui and L. Drăguț, "Random forest in remote sensing: A review of applications and future directions," *ISPRS J. Photogramm. Remote Sens.*, vol. 114, pp. 24–31, Apr. 2016, doi: [10.1016/j.isprsjprs.2016.01.011](https://doi.org/10.1016/j.isprsjprs.2016.01.011).
- [34] X. Liu *et al.*, "Downscaling of solar-induced chlorophyll fluorescence from canopy level to photosystem level using a random forest model," *Remote Sens. Environ.*, vol. 231, Sep. 2019, Art. no. 110772, doi: [10.1016/j.rse.2018.05.035](https://doi.org/10.1016/j.rse.2018.05.035).
- [35] J. Ju, D. P. Roy, E. Vermote, J. Masek, and V. Kovalevskyy, "Continental-scale validation of MODIS-based and LEDAPS landsat ETM+ atmospheric correction methods," *Remote Sens. Environ.*, vol. 122, pp. 175–184, Jul. 2012, doi: [10.1016/j.rse.2011.12.025](https://doi.org/10.1016/j.rse.2011.12.025).
- [36] H. K. Zhang *et al.*, "Characterization of sentinel-2A and Landsat-8 top of atmosphere, surface, and Nadir BRDF adjusted reflectance and NDVI differences," *Remote Sens. Environ.*, vol. 215, pp. 482–494, Sep. 2018, doi: [10.1016/j.rse.2018.04.031](https://doi.org/10.1016/j.rse.2018.04.031).
- [37] Y. Sun, Q. Qin, H. Ren, T. Zhang, and S. Chen, "Red-edge band vegetation indices for leaf area index estimation from Sentinel-2/MSI imagery," *IEEE Trans. Geosci. Remote Sens.*, vol. 58, no. 2, pp. 826–840, Feb. 2020, doi: [10.1109/TGRS.2019.2940826](https://doi.org/10.1109/TGRS.2019.2940826).
- [38] I. Herrmann, A. Pimstein, A. Karnieli, Y. Cohen, V. Alchanatis, and D. J. Bonfil, "LAI assessment of wheat and potato crops by VEN μ S and Sentinel-2 bands," *Remote Sens. Environ.*, vol. 115, no. 8, pp. 2141–2151, Aug. 2011, doi: [10.1016/j.rse.2011.04.018](https://doi.org/10.1016/j.rse.2011.04.018).
- [39] L. Korhonen, P. Packalen, and M. Rautiainen, "Comparison of Sentinel-2 and Landsat 8 in the estimation of boreal forest canopy cover and leaf area index," *Remote Sens. Environ.*, vol. 195, pp. 259–274, Jun. 2017, doi: [10.1016/j.rse.2017.03.021](https://doi.org/10.1016/j.rse.2017.03.021).

- [40] Y. Sun, H. Ren, T. Zhang, C. Zhang, and Q. Qin, "Crop leaf area index retrieval based on inverted difference vegetation index and NDVI," *IEEE Geosci. Remote Sens. Lett.*, vol. 15, no. 11, pp. 1662–1666, Nov. 2018, doi: [10.1109/LGRS.2018.2856765](https://doi.org/10.1109/LGRS.2018.2856765).
- [41] D. Xu, D. An, and X. Guo, "The impact of non-photosynthetic vegetation on LAI estimation by NDVI in mixed grassland," *Remote Sens.*, vol. 12, no. 12, p. 1979, Jun. 2020, doi: [10.3390/rs12121979](https://doi.org/10.3390/rs12121979).
- [42] T. Hilker, A. I. Lyapustin, C. J. Tucker, P. J. Sellers, F. G. Hall, and Y. Wang, "Remote sensing of tropical ecosystems: Atmospheric correction and cloud masking matter," *Remote Sens. Environ.*, vol. 127, pp. 370–384, Dec. 2012, doi: [10.1016/j.rse.2012.08.035](https://doi.org/10.1016/j.rse.2012.08.035).
- [43] J. Hu *et al.*, "Performance of the MISR LAI and FPAR algorithm: A case study in Africa," *Remote Sens. Environ.*, vol. 88, no. 3, pp. 324–340, Dec. 2003, doi: [10.1016/j.rse.2003.05.002](https://doi.org/10.1016/j.rse.2003.05.002).
- [44] H. Fang *et al.*, "Characterization and intercomparison of global moderate resolution leaf area index (LAI) products: Analysis of climatologies and theoretical uncertainties," *J. Geophys. Res., Biogeosci.*, vol. 118, no. 2, pp. 529–548, Jun. 2013, doi: [10.1002/jgrg.20051](https://doi.org/10.1002/jgrg.20051).
- [45] H. Jiang, N. Lu, J. Qin, W. Tang, and L. Yao, "A deep learning algorithm to estimate hourly global solar radiation from geostationary satellite data," *Renew. Sustain. Energy Rev.*, vol. 114, Oct. 2019, Art. no. 109327, doi: [10.1016/j.rser.2019.109327](https://doi.org/10.1016/j.rser.2019.109327).
- [46] Y. Park, B. Kwon, J. Heo, X. Hu, Y. Liu, and T. Moon, "Estimating PM_{2.5} concentration of the conterminous united states via interpretable convolutional neural networks," *Environ. Pollut.*, vol. 256, Jan. 2020, Art. no. 113395, doi: [10.1016/j.envpol.2019.113395](https://doi.org/10.1016/j.envpol.2019.113395).
- [47] X. Wang, J. Huang, Q. Feng, and D. Yin, "Winter wheat yield prediction at county level and uncertainty analysis in main wheat-producing regions of China with deep learning approaches," *Remote Sens.*, vol. 12, no. 11, p. 1744, May 2020, doi: [10.3390/rs12111744](https://doi.org/10.3390/rs12111744).
- [48] G. Gao and Y. Gu, "Multitemporal landsat missing data recovery based on tempo-spectral angle model," *IEEE Trans. Geosci. Remote Sens.*, vol. 55, no. 7, pp. 3656–3668, Jul. 2017, doi: [10.1109/TGRS.2017.2656162](https://doi.org/10.1109/TGRS.2017.2656162).
- [49] Q. Zhang, Q. Yuan, C. Zeng, X. Li, and Y. Wei, "Missing data reconstruction in remote sensing image with a unified spatial-temporal-spectral deep convolutional neural network," *IEEE Trans. Geosci. Remote Sens.*, vol. 56, no. 8, pp. 4274–4288, Aug. 2018, doi: [10.1109/TGRS.2018.2810208](https://doi.org/10.1109/TGRS.2018.2810208).
- [50] K. A. Adepoju and S. A. Adelabu, "Improving accuracy of Landsat-8 OLI classification using image composite and multisource data with Google Earth engine," *Remote Sens. Lett.*, vol. 11, no. 2, pp. 107–116, Feb. 2020, doi: [10.1080/2150704X.2019.1690792](https://doi.org/10.1080/2150704X.2019.1690792).
- [51] M. Claverie *et al.*, "The harmonized landsat and Sentinel-2 surface reflectance data set," *Remote Sens. Environ.*, vol. 219, pp. 145–161, Dec. 2018, doi: [10.1016/j.rse.2018.09.002](https://doi.org/10.1016/j.rse.2018.09.002).



Yuanheng Sun received the B.S. degree from East China Normal University, Shanghai, China, in 2015. He is pursuing the Ph.D. degree with the School of Earth and Space Sciences, Peking University, Beijing, China.

His research interests include remote sensing of vegetation and its response to global climate change.



Qiming Qin received the B.S. degree in geography from Nanjing Normal University, Nanjing, China, in 1982, the M.S. degree in geophysics from Shaanxi Normal University, Xi'an, China, in 1987, and the Ph.D. degree in geophysics from Peking University, Beijing, China, in 1990.

He is a Professor with the Institute of Remote Sensing and Geographic Information System, School of Earth and Space Sciences, Peking University. He also serves as the Secretary General of the National Steering Committee for Geography Education in universities and colleges, China, and the Remote Sensing Application Consortium of universities and colleges, China.

Dr. Qin is the Executive Director of the Environmental Remote Sensing Commission of the Geographical Society of China and the Director of the China Association for Geographic Information System, the Chinese Society for Geodesy, Photogrammetry and Cartography, the China Hi-Tech Industrialization Association, and the Chinese Association of Young Scientists and Technicians. He has served as an Evaluator of the Domestic GIS Software Evaluation Expert Team of the China Association for Geographic Information System in 1996 and a Lead Evaluator of the GIS Software Evaluation Committee of the Ministry of Science and Technology of China in 1995.



Huazhong Ren received the Ph.D. degree from Beijing Normal University, Beijing, China, and Université de Strasbourg, Strasbourg, France, in 2013.

Since 2016, he has been an Assistant Professor with the Institute of Remote Sensing and Geographic Information System, School of Earth and Space Sciences, Peking University, Beijing. His research interests focus on land surface temperature/emissivity estimate from thermal infrared remote sensing data.



Yao Zhang received the Ph.D. degree from China Agricultural University, Beijing, China, in 2017.

She is an Associate Professor with the Key Laboratory of Modern Precision Agriculture System Integration Research, Ministry of Education, China Agricultural University. Her research focuses on smart agriculture and quantitative remote sensing. The research topics include crop growth status monitoring and soil nutritional detection and sensor development.